

# High-temperature tribological property of Fe-based amorphous alloy coating

Jun-jie Xu<sup>a</sup>, Jia-jie Kang<sup>a,b,c,d,\*</sup>, Wen Yue<sup>a,c</sup>, Zhi-qiang Fu<sup>a,c</sup>, Li-na Zhu<sup>a,c</sup>, Ding-shun She<sup>a,c</sup>

<sup>a</sup> School of Engineering and Technology, China University of Geosciences (Beijing), Beijing, 100083, PR China

<sup>b</sup> Institute of Flexible Electronics Technology of Tsinghua, Zhejiang, Jiaxing, 314000, PR China

<sup>c</sup> Zhengzhou Research Institute, China University of Geosciences (Beijing), Zhengzhou, 451283, PR China

<sup>d</sup> State Key Laboratory of Tribology, Department of Mechanical Engineering, Tsinghua University, Beijing, 100084, PR China

## ARTICLE INFO

### Keywords:

Spraying  
Fe-based amorphous alloy coating  
High-temperature tribological  
Wear mechanism

## ABSTRACT

Two kinds of Fe-based amorphous alloy coatings were fabricated by high velocity oxygen fuel (HVOF) spraying and cold spraying (CS). Microstructure, amorphous content, hardness, and high-temperature (below the glass transition temperature) tribological performance were investigated. Results show that the Fe-based amorphous coatings prepared by CS have a high hardness and a low wear rate at room temperature. At 673 K, the oxide layer grew, broke, and peel off periodically, resulting in a high wear rate. Moreover, the high-temperature wear mechanism was fatigue, adhesive, and oxidative wear. Meanwhile, the different crystallization and oxidation behavior of CS and HVOF coatings resulting in the different wear rates at 673 K.

## 1. Introduction

Amorphous alloys (also known as metallic glasses) have been one of the most popular frontiers of research since they were developed in 1960. In the process of preparation using ultra-rapid cold solidification techniques, the atoms in the molten alloy are not ready to crystallize in an orderly arrangement, so the obtained solid alloy has a short- and medium-range ordered structure and a long-range disordered structure of internal atoms, without the grains and grain boundaries of crystalline alloys [1–4]. The unique structure gives amorphous alloys excellent physical, chemical, and mechanical properties and is expected to be a key structural material in aerospace equipment, biomedical devices, precision equipment, and other fields. Among them, Fe-based amorphous alloys have become the focus of research and development in the materials science community due to their ultra-high-strength and hardness, excellent wear and corrosion resistance, superior soft magnetic properties, and low economic cost [5–7]. However, the limited glass-forming ability (GFA) and inherent brittleness of amorphous alloys severely limit the engineering applications of Fe-based amorphous alloys. Fortunately, the preparation of amorphous coatings by thermal spray techniques (including high velocity oxygen fuel [8], high velocity air fuel [9], plasma spraying [10], arc spraying [11], and cold spraying [12,13]) can overcome these problems and become an effective way to

protect the material surface. For example, Yasir et al. [14] blended 20% wt. of Al<sub>2</sub>O<sub>3</sub> powder in Fe-based amorphous powder and found that the composite coatings had a very low friction factor (<0.2) and the wear resistance of the coating was two to three times that of the pure amorphous coating. Su et al. [15] prepared Fe-based amorphous coatings by cold spraying and HVOF spraying methods, and the results showed that the cold spraying method could prepare dense amorphous coatings with excellent wear resistance.

In the HVOF thermal spraying process, the raw material powder is injected into the gun, heated to a molten or semi-molten state, accelerated toward the substrate, and then diffused laterally and cured rapidly [16]. Among the various thermal spraying techniques, HVOF thermal spraying is reported to have several advantages; for example, high productivity and excellent properties such as high densities, low porosity, high bond strength, and low residual stresses in the prepared coatings. The process of cold spraying technology is that a high pressure gas preheated at a certain low temperature is passed through a scaled nozzle to produce a supersonic gas flow jet, which accelerates the sprayed particles by sending them axially into the gas jet to form a coating by impacting the substrate as a solid state [17]. Unlike the traditional thermal spraying technology, the cold spraying process temperature is lower than the melting point of the sprayed particles, and the particles do not go through the melting-re-solidification process

\* Corresponding author.

E-mail address: [kangjiajie@cugb.edu.cn](mailto:kangjiajie@cugb.edu.cn) (J.-j. Kang).

<https://doi.org/10.1016/j.jnoncrysol.2021.121136>

Received 25 May 2021; Received in revised form 13 August 2021; Accepted 19 August 2021

Available online 2 September 2021

0022-3093/© 2021 Elsevier B.V. All rights reserved.

during the spraying process, which avoids oxidation and crystallization in the preparation of amorphous coatings, and improves the compressive stress and metallurgical bonding with the substrate.

The wear behavior of amorphous coatings is extremely sensitive to wear test parameters (e.g., applied load, temperature, and sliding distance), and the contact temperature (flash temperature) of the sliding surface may exceed the glass transition temperature and crystallization temperature even at room temperature wear tests, leading to viscous flow and nanocrystallization-induced wear mechanisms [15,18–20]. Li et al. [21] investigated the wear behavior of sprayed Fe-based amorphous coatings. The results showed that the coating wear rate was more sensitive to sliding velocity than to normal loading, and the wear mechanisms were mainly oxidation wear and delamination wear. Although the room-temperature wear behavior of Fe-based amorphous alloy coatings has been studied extensively, there are few reports on the high-temperature wear behavior [22].

In this paper, Fe-Cr-Mo-C-B-Y system amorphous coatings were prepared on 35CrMo steel substrate using HVOF and CS techniques, and the high-temperature (below the glass transition temperature) tribological properties of Fe-based amorphous coatings at different temperatures (293 K, 473 K, 673 K) were systematically discussed by conducting ball-plate linear sliding tests, comparing HVOF coatings and CS coatings. The differences in wear mechanisms between HVOF and CS coatings were compared.

## 2. Material and methods

### 2.1. Material and specimen preparation

In this work, the raw material powder used was a Fe-based amorphous alloy powder prepared by high-pressure inert gas atomization method with a composition content of  $\text{Fe}_{48}\text{Cr}_{15}\text{Mo}_{14}\text{C}_{15}\text{B}_6\text{Y}_2$  at.%. The amorphous powder with a particle size distribution of 10–30  $\mu\text{m}$  was screened for the preparation of the coating by cold spraying technology, and the powder with a particle size distribution of 25–58  $\mu\text{m}$  was screened for the preparation of the coating by supersonic flame spraying technology. The substrate material used for the coating is 35CrMo alloy structural steel. The sample was machined by EDM wire cutting into a block of 50 mm  $\times$  15 mm  $\times$  5 mm in size, and C1 chamfering was done to facilitate assembly and to prevent the coating from cracking due to stress concentration during the experiment. Before spraying, the substrate surface was de-oiled and sandblasted to increase the surface roughness and thus improve the bonding strength of the coating and the substrate. The blasting material is diamond sand with the size of 250–800  $\mu\text{m}$ , the blasting pressure is 0.9 bar, the blasting time is 30 s, and the blasting distance is 30 mm. CS technology uses the spraying equipment from Impact, Germany, model No. Impact 5/11.

The technical parameters of the spraying are shown in Table 1. HVOF amorphous coating of about 250  $\mu\text{m}$  and CS amorphous coating of 900  $\mu\text{m}$ , respectively, were prepared on the substrate surface. Scanning electron microscopy (SEM) and energy-dispersive X-ray spectroscopy (EDS) were used to observe and analyze the microscopic morphology and elemental species and distribution information of the powders and coatings. The SEM uses the  $\text{SE}_2$  signal channel with an operating voltage of 15 kV. The porosity of the coatings was calculated by grayscale processing of SEM images of the coating cross-sections using the image processing software ImageJ2X and averaging the measurements over

**Table 1**  
CS and HVOF process parameters.

CS process		HVOF process	
Gas pressure (MPa)	4.5	Spraying distance (mm)	240
Gas temperature ( $^{\circ}\text{C}$ )	900	Shroud gas (NLPM)	354
Spraying distance (mm)	20	Oxygen (NLPM)	200
Powder feeder rate (rpm)	3	Hydrogen (NLPM)	600

multiple ( $\leq 10$ ) selected areas. The composition and phase composition of the powders and coatings were analyzed by using an X-ray diffractometer (XRD) equipped with Cu  $\text{K}\alpha$  rays at a scanning speed of  $4^{\circ}/\text{min}$ , continuous scanning, and a scanning angle of 20–80 $^{\circ}$ . The amorphous content of the powders and coatings was also fitted semi-quantitatively on MDI Jade 6.0 software based on the reference intensity method (RIR). A differential thermal analyzer (DTA) was used to analyze the thermal stability and crystallization temperature of the powders and coatings. The temperature range was 373–1073 $^{\circ}\text{C}$ , and the heating rate was 10 K/min. Argon was chosen as the protective atmosphere. Differential thermal analysis is a method of thermal analysis by measuring the temperature difference between the sample and the reference ratio as a function of temperature, which can be used to obtain the characteristic temperature of amorphous crystallization by heat absorption or exothermic changes. A microhardness tester was used to measure the coating's microhardness. The load was set at 3 N and the ballast holding time was 15 s. The measurement was performed by pressing a square conical diamond indenter with a top angle of 136 $^{\circ}$  into the coating cross-section and calculating the hardness value at the measured point by measuring the average length of the diagonal on the diamond-shaped indentation using the Vickers hardness formula  $\text{HV} = 1854.4 L/d^2$  (HV0.3), where  $L$  is the load and  $d$  is the diagonal length. In the vertical direction, with the bond between the coating and the substrate as 0, positive towards the coating and negative towards the substrate, points are taken every 50  $\mu\text{m}$  for HVOF coatings and every 100  $\mu\text{m}$  for CS coatings, hitting from the near surface of the coating to the substrate. Three points are taken in the horizontal direction, and the average hardness value of the three tests is used as the hardness at that depth. Avoid the defective area when making the points.

### 2.2. Wear test

The test was conducted using the UMT multifunctional wear tester. The coating was subjected to a high temperature reciprocating sliding experiment by loading a high temperature module under high temperature conditions. Before the experiment, the surface of the coating was polished. The parameters of the high-temperature wear test were set as follows: 293 K, 473 K, 673 K. Silicon nitride of  $\Phi 6$  was used for the grinding ball, normal load 10 N, frequency 10 Hz, test time 1800 s, stroke 6 mm, and a new silicon nitride for the grinding ball was used for each experiment. Each parameter was repeated three times to obtain the average value to increase the reliability of the experiment. The effect of different temperatures on the sliding friction wear of the coating was investigated, and the wear mechanism of the coating at different parameters was explored. All samples were ultrasonically cleaned with ethanol and then dried before capturing the three-dimensional (3D) morphology of the wear trajectory by optical profilometry. Subsequently, precise wear volumes were obtained by analyzing 3D wear images. Three contouring trajectories were measured on each wear surface. The volume loss before and after the wear experiment was also used to characterize the wear rate, which was calculated as follows:  $Q = \frac{V_w}{NS}$ , where  $Q$  is the wear rate ( $\text{mm}^3 \cdot \text{N}^{-1} \cdot \text{m}^{-1}$ ),  $V_w$  is the wear volume ( $\text{mm}^3$ ) obtained by integrating the cross-sectional profile of the wear traces, and  $N$  and  $S$  denote the applied load (N) and the total travel distance (mm), respectively [23].

## 3. Results

### 3.1. Characteristics of the powders and coatings

Fig. 1 shows the scanning electron microscopy secondary electron images of the powders (raw material powders of CS and HVOF, respectively). As shown in Fig. 1(a), the diameters of the CS raw material powders are about 10–30  $\mu\text{m}$ , and most of them are spherical with smooth surfaces, and some of the particles have satellite balls attached

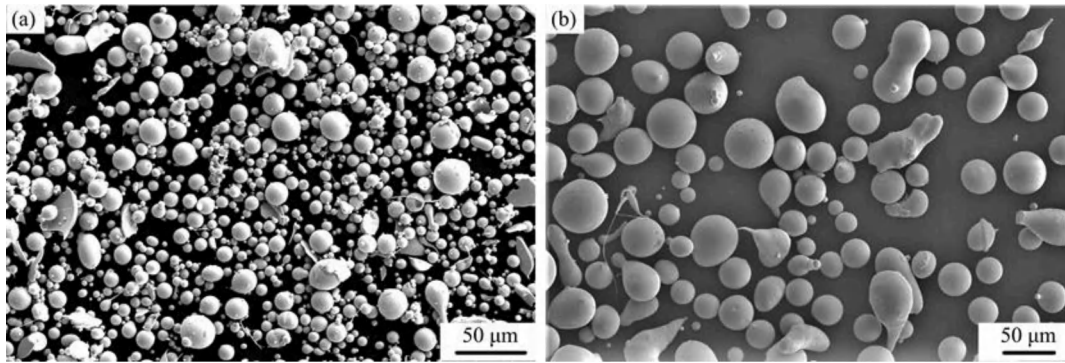


Fig. 1. Secondary electron SEM image of Fe-based amorphous feedstock powders: (a) CS powders; (b) HVOF powders.

to them. As shown in Fig. 1(b), the diameter of HVOF raw material powder is about 20~60  $\mu\text{m}$ , with an ellipsoidal or irregular shape and relatively smooth surface.

Fig. 2 shows the physical phase analysis of the raw material powder and coating. Analyzing the XRD characterization results of the powders, it can be found that both CS and HVOF powders have obvious amorphous peaks in the region of  $2\theta = 40\sim 50^\circ$ , indicating the presence of amorphous phases, while CS powder has several crystalline diffraction peaks overlapping the amorphous peaks and HVOF powder contains  $\text{Mo}_2\text{B}$ ,  $\text{Mo}_2\text{C}$  crystalline peaks at  $2\theta = 39\sim 42^\circ$ . The two powders exhibit a mixed structure of amorphous and crystalline phases. Comparing the XRD physical phase results of the coating, it can be found that the CS coating has a bun peak and no obvious crystalline diffraction peak, and the amorphous content of the coating is about 90% after fitting calculation using MDI-Jade 6.0 software, which has a high amorphous content. The HVOF coating has an overall amorphous phase with an amorphous content of about 85%, which is lower than the CS coating, due to the high temperature in the spraying process and some of the crystalline phases  $\text{C}_2\text{Cr}_3$ ,  $\text{Cr}_{23}\text{C}_6$  precipitated during the spraying process [24].

Fig. 3 shows the microscopic morphology of the surface and cross-section of CS and HVOF coatings, respectively. As seen in Fig. 3(a), the surface of CS coating is made up of partially deformed powder particles, because the powder particles remain solid during the cold spraying process, and when their movement speed exceeds the critical speed, the interface between the particles and the substrate generates adiabatic shear instability, which causes the particles to undergo severe plastic deformation and deposit on the workpiece surface [25]. Fig. 3(d) shows the surface morphology of HVOF coating, which shows that the coating surface is molten and the unmelted particles on the surface are less and the whole is more complete. Fig. 3 (b & c) shows the cross section of CS coating. It can be seen that the CS coating has no obvious cracks and is well bonded to the substrate with a coating thickness of about 900

$\mu\text{m}$ . From Fig. 3(c), it can be seen that there are some small pores inside the coating due to the incomplete bonding of the particles during the deposition process [26]. The coating and substrate are found to bite each other at the bonding interface of the coating and substrate, which indicates that the deposition mechanism of the coating is mechanical deposition. The coating cross-section was selected several times using ImageJ2x software and grayed out, and the obtained coating porosity was about 1.3%, indicating that the coating structure was dense. Fig. 3(e & f) shows the cross-sectional morphology of the HVOF coating. The coating has a layer-by-layer stacked structure, which is a typical thermal spraying laminate structure. The interface between the coating and the substrate is clear, and the thickness of the coating is about 250  $\mu\text{m}$ . The measured porosity of the coating is about 2%. Two main reasons can lead to porosity: the layer stacking laminate structure can create large porosity, and the molten droplets shrink partially due to cooling and make the gas not expelled to form small porosity [27].

### 3.2. Mechanical properties of Fe-based amorphous coatings

Fig. 4 shows the microhardness distribution curves of CS and HVOF coatings along the cross section. The average hardness of the CS coating is about 1005.5HV0.3 and the maximum hardness is 1104HV0.3, which is 3.9 times higher than that of the base 35CrMo (283HV0.3) and significantly higher than that of the HVOF coating at 935.5HV0.3. The ultra-hardness of the Fe-based amorphous alloy coating comes from the diffusion strengthening of the metal carbide and the formation of the amorphous phase. It can be seen that CS coatings exhibit higher hardness due to higher amorphous content [28,29].

Fig. 5 shows the DTA curves of CS and HVOF coatings, both of which exhibit multi-stage exothermic properties. The crystallization temperature of the HVOF coating is about 690°C and that of CS is about 720°C, which indicates that the transformation of the amorphous phase in the coating occurs above the crystallization temperature. Compared with

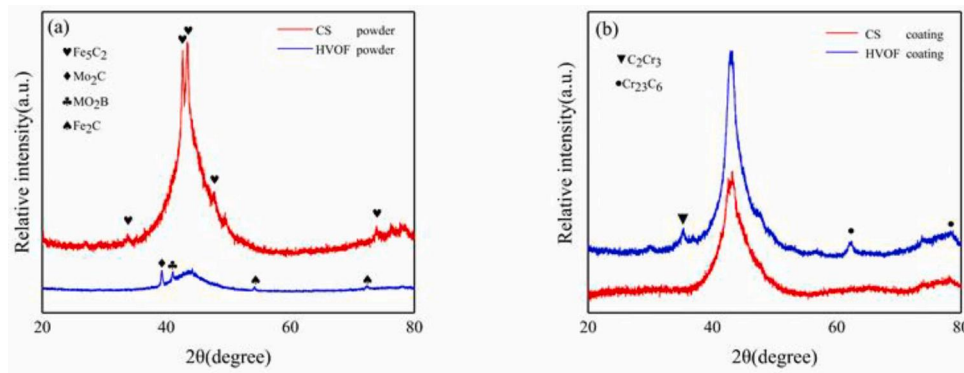


Fig. 2. XRD patterns of the Fe-based amorphous powders and sprayed coatings, (a) powders; (b) coatings.

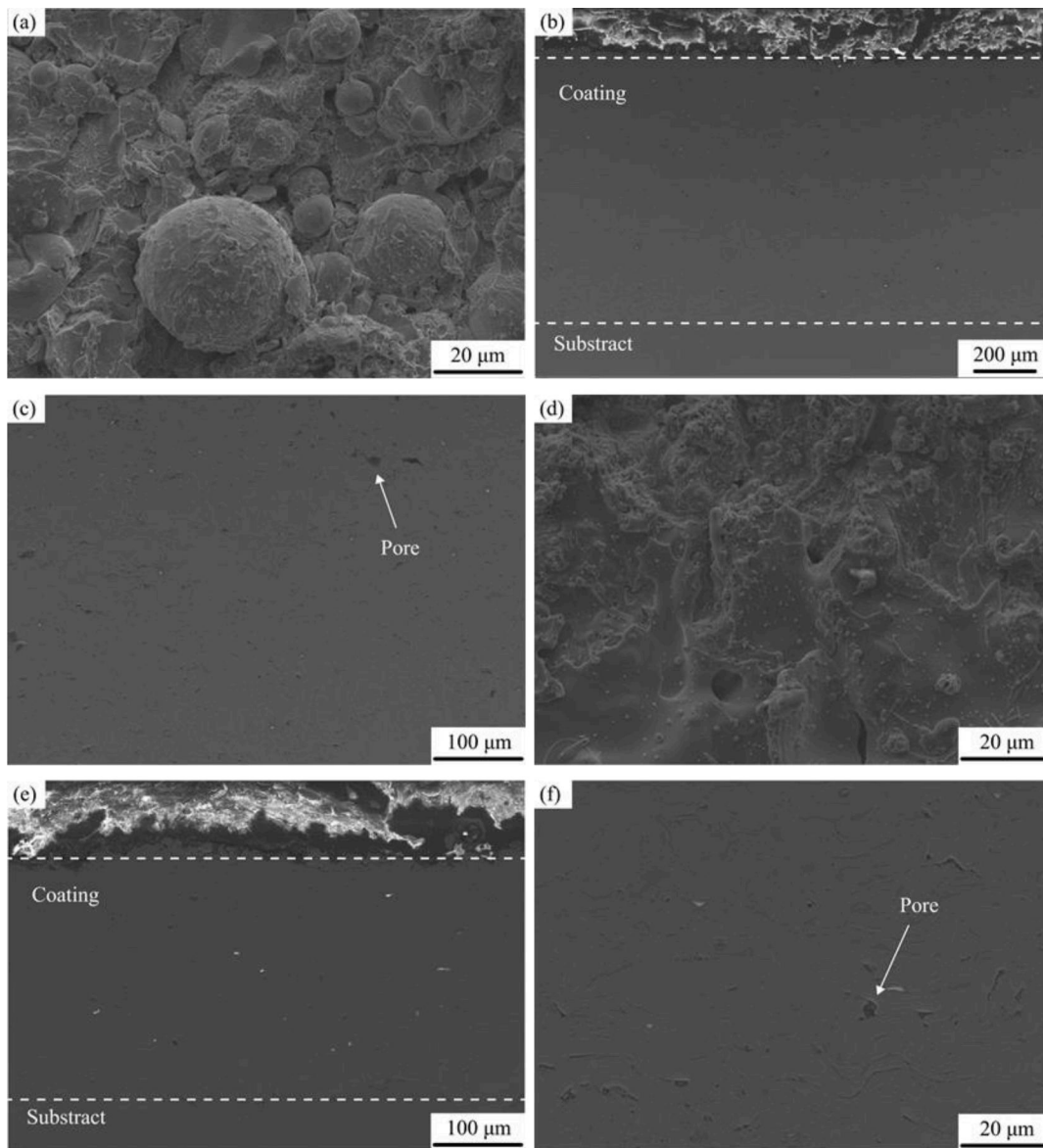


Fig. 3. SEM images of Fe-based amorphous coatings, (a) The surface of CS coating, (b) The cross-section of CS coating, (c) The magnification of cross-section of CS coating; (d) The surface of HVOF coating, (e) The cross-section of HVOF coating, (f) The magnification of cross-section of HVOF coating.

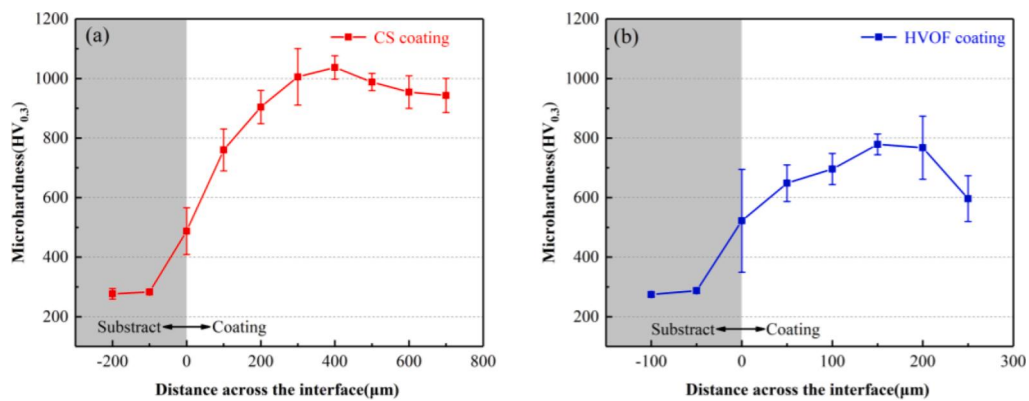


Fig 4. Microhardness–distance profile of Fe-based amorphous sprayed coatings, (a) CS coating; (b) HVOF coating.

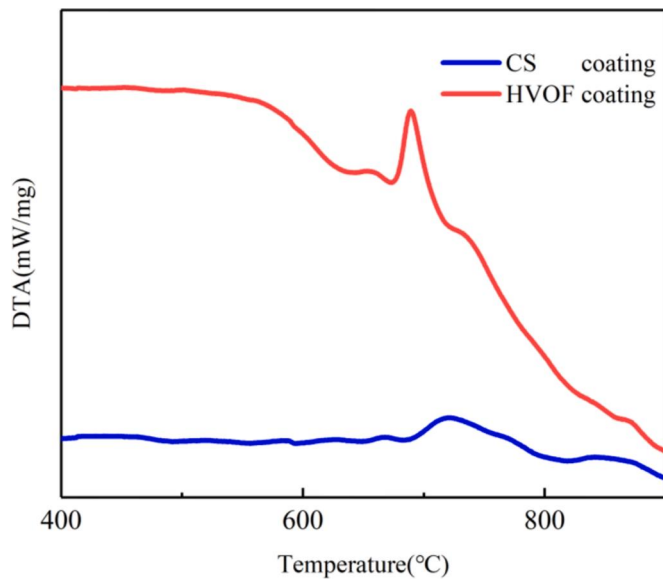


Fig. 5. DTA date of Fe-based amorphous coatings.

the HVOF coating, the initial crystallization temperature and rapid exothermic temperature of the CS coating are slightly higher than those of the HVOF coating, which has better thermal stability [30].

### 3.3. Tribological performance of Fe-based amorphous coating at elevated temperature

The tribological properties of the materials are influenced by multiple factors, such as pressure, load, sliding speed, and test temperature. Fig. 6 shows the average friction coefficient of the two coatings as a function of temperature. It can be seen from the figure that the average COF of both CS and HVOF coatings increases with the increase of temperature. As the temperature rises from room temperature to 673 K, the COF curve of CS coating rises significantly more than that of HVOF coating, and the average COF of CS coating is larger than that of HVOF coating at 673 K. The change of COF reflects the evolution of surface microstructure.

From Fig. 6, it can be found that the curves can be divided into two stages, namely the break-in stage and the steady-state stage. the COF values increase sharply in the break-in stage and then drop rapidly to near the steady-state friction coefficient, which is due to the different surface roughness and the constant adjustment of the friction process with the change of the contact surface [31]. During the break-in period, the micro-convexity of the contact surface is crushed and the contact

area increases and a dynamic balance is formed between the formation and removal of the oxide layer during the steady-state period, with the friction coefficient fluctuating within a certain range. The rapid decrease after the initial peak comes from the generation of low shear transfer films during the friction process.

Fig. 7 shows the three-dimensional morphology of the local wear marks of  $\text{Si}_3\text{N}_4$  after a reciprocal sliding friction experiment with a load of 10 N for 1800 s on both coatings.

Fig. 8 corresponds to the wear surface profiles of both coatings at different temperatures. It can be found that the wear depth increases with the increase of temperature. At 673 K, the wear depth of CS coating is about 16  $\mu\text{m}$  and that of HVOF is about 12  $\mu\text{m}$ .

The wear volume is obtained by integrating the surface profile of the wear marks using a 3D white light interferometer, as shown in Fig. 9(b), which shows the wear rate calculated using the equation  $Q = \frac{V_w}{NS}$ . The wear rate of CS coating is the largest at 673 K, which is the wear rate of HVOF coating is maximum at 673 K with  $1.70 \times 10^{-5} \text{ mm}^3 \cdot \text{m}^{-1} \cdot \text{N}^{-1}$ . The wear volume growth rate of CS coating is higher than that of HVOF coating at 293 K, 473 K, and 673 K. At 273 K, the wear rate of CS coating is about 3/5 of that of HVOF coating, which shows excellent wear resistance, and the wear rate of the CS coating was about 1.3 times that of the HVOF coating when the ambient temperature increased to 673 K. Thus, the HVOF coating exhibits better sliding wear resistance than the CS coating under high temperature conditions.

### 3.4. Wear mechanism of Fe-based amorphous coating under various conditions

In order to analyze the high temperature wear mechanism of the Fe-based amorphous alloy coatings, the wear morphology of the coatings was characterized using SEM/EDS. Fig. 10 shows the microscopic morphology of the wear marks. It can be seen from the figures that microploughs and pits exist on the wear surface of the CS coating at 293 K, and are accompanied by areas partially covered by bright particles, indicating that abrasive wear has occurred [32]. Because of the dense structure and relatively high hardness of the CS coating, the coating surface is not easy to crack and peel, and oxidative wear is the main wear mechanism of the CS coating at 293 K [15]. In addition, a large number of cracks and pits were found in the wear traces of the CS coating at 673 K. This is due to the cracking of the Fe-based amorphous alloy coating under the action of shear force, and the instantaneous release of energy accumulated by friction during the transient crack expansion, which causes the local amorphous coating to melt or flake off and detach from the coating with the friction sub [33].

From the microscopic morphology of the HVOF coating at 293 K (Fig. 11), it can be found that the wear surface is rougher, with a large number of deep grooves, pits, and attached debris. The fatigue wear becomes the main wear mechanism of the HVOF coating at 293 K. It is

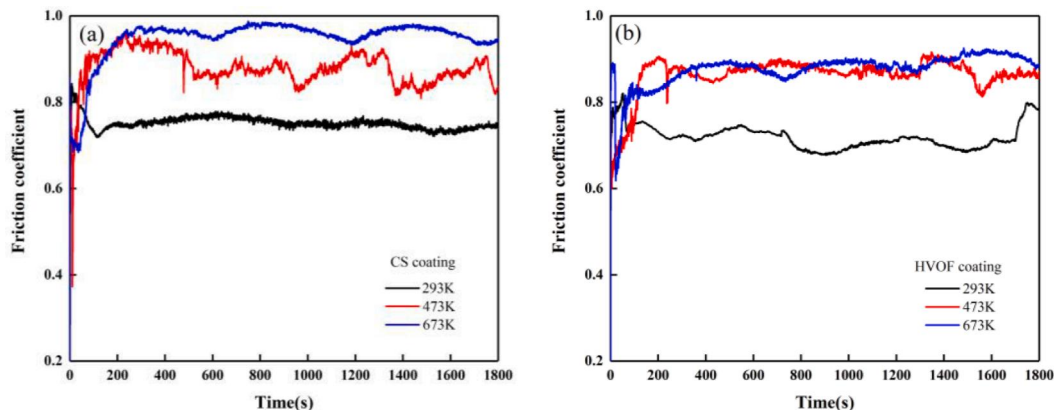


Fig. 6. Friction coefficient versus sliding time curves of Fe-based amorphous sprayed coatings, (a) CS coating, and (b) HVOF coating.

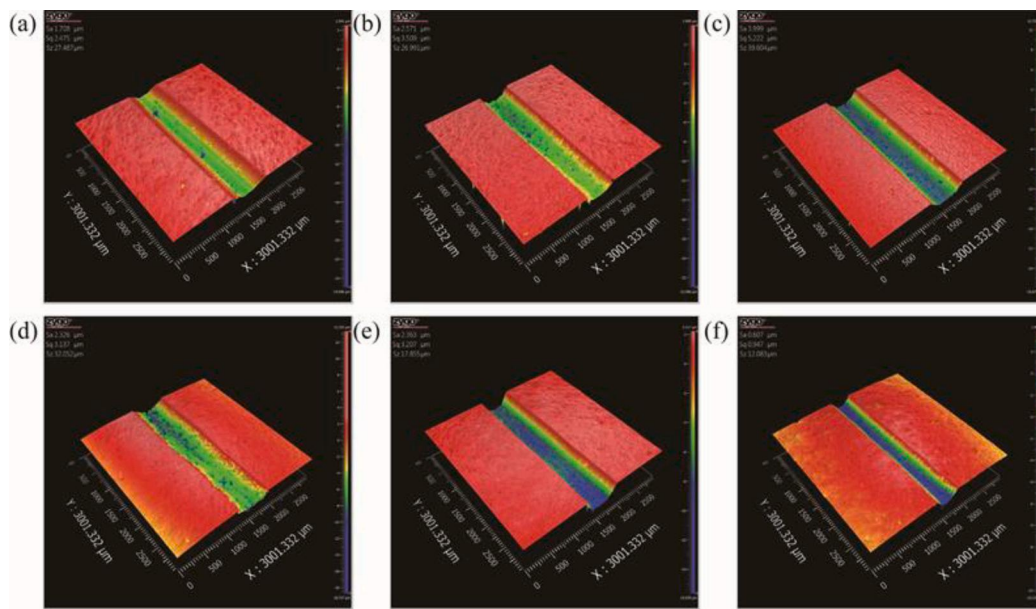


Fig. 7. Wear scar morphologies of track width of Fe-based amorphous coatings, (a) CS coating, 293 K; (b) CS coating, 473 K; (c) CS coating, 673 K; (d) HVOF coating, 293 K; (e) HVOF coating, 473 K; (f) HVOF coating, 673 K.

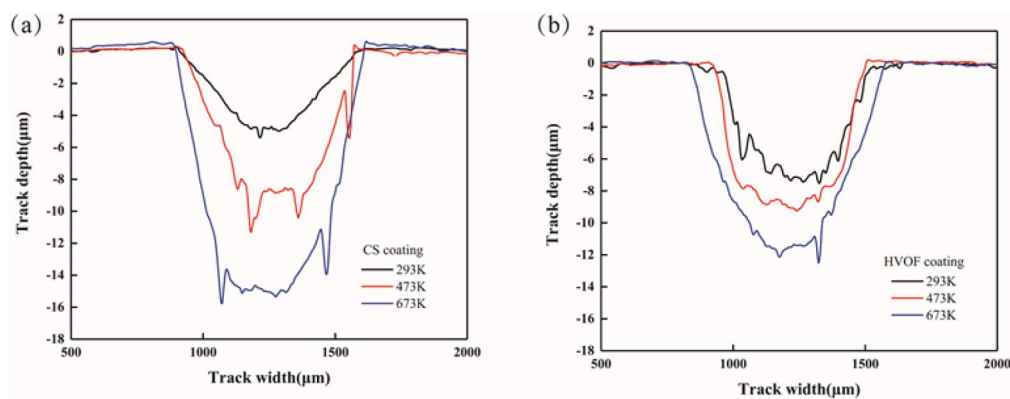


Fig. 8. Track depth in the function of track width of Fe-based amorphous coatings, (a) CS coating; (b) HVOF coating.

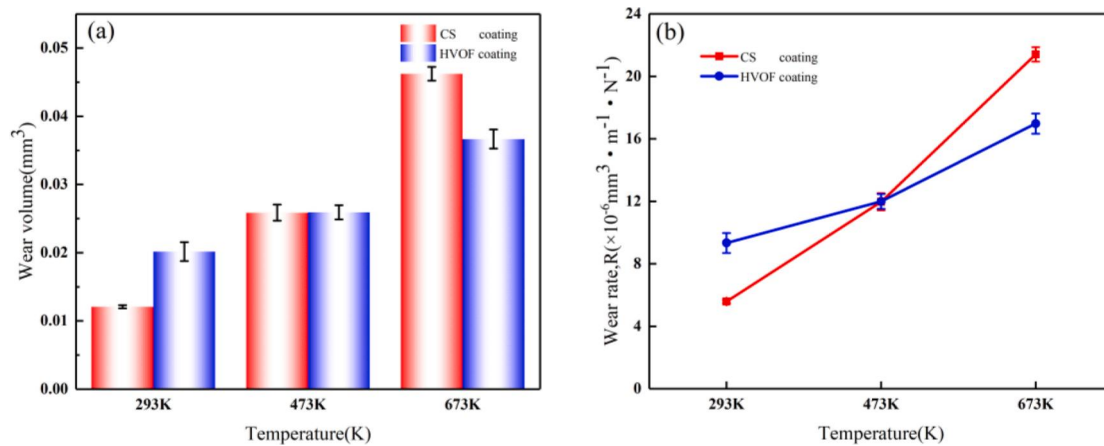


Fig. 9. (a) wear volume and (b) wear rate of CS coating and HVOF coating under various sliding conditions.

known that the HVOF coating has a layer-by-layer stacked structure, and the amorphous coating is stripped by repeated plowing fatigue [11,34].

It is well known that Fe, Mo, and other elements in Fe-based

amorphous alloy coatings are highly susceptible to oxidation at high temperatures [35]. In general, the oxidation reaction is mainly the inward diffusion of oxygen into the amorphous substrate, and defective

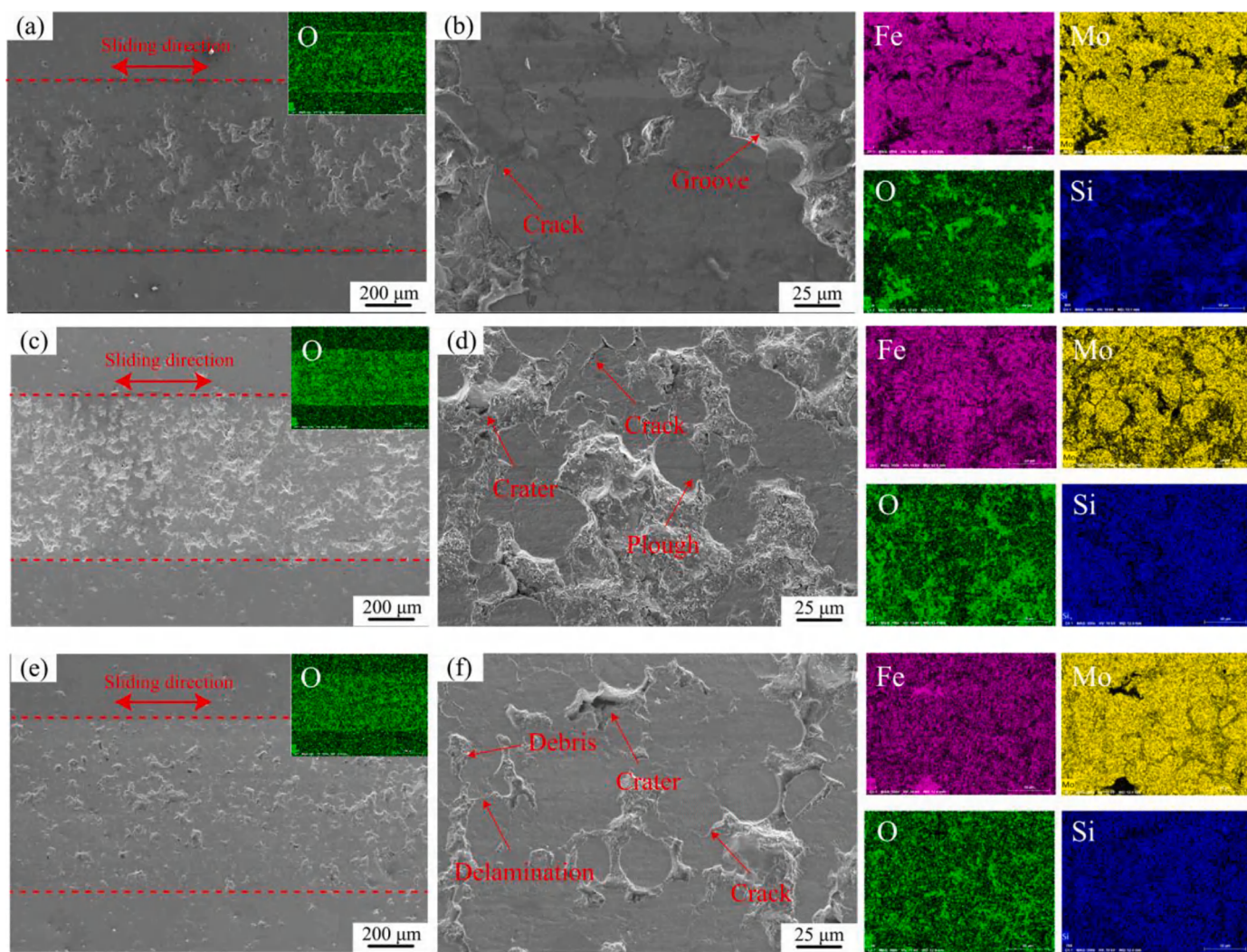


Fig. 10. worn morphologies of CS coating under various conditions: (a,b) 293 K; (c,d) 673 K; (e,f) 673 K.

areas in the coating, including pores and cracks, will become the preferred channels for the diffusion of oxygen elements [36]. For amorphous alloy coatings, as the sliding conditions change, the friction surface contact temperature, i.e., the flash point temperature, increases, and the contact flash point temperature between the Fe-based amorphous alloy coating and  $\text{Si}_3\text{N}_4$  on the grinding ball under high temperature conditions will reach and exceed the glass transition temperature and crystallization temperature, leading to viscous flow and amorphous crystallization [37]. As seen in Figs. 3–9(f), the CS coating surface under 673 K friction test conditions exhibits the coexistence of relatively smooth areas and rough areas, with a large number of fragments flaking off and adhering to the wear surface during sliding, indicating increased fatigue wear.

Meanwhile, the EDS results in Fig. 10 show that in addition to Fe, Mo, C, and Cr elements, there are accompanying O and Si elements. The metallic elements in the coating such as Fe, Cr, and Mo react with oxidation at high temperatures to form an oxide layer, which grows to a critical thickness with continuous high-temperature sliding friction and ruptures due to brittleness or accumulation of residual stress, eventually leading to the oxide layer peeling off the coating surface as well as some oxide fragments adhering to the surface, and the periodic growth, rupture, and peeling of the oxide layer makes it have a high wear rate at high temperatures. The oxide layer grows, breaks and peels off periodically, resulting in a high wear rate at high temperatures. Since  $\text{Si}_3\text{N}_4$  was chosen for the grinding balls, the presence of Si elements indicates the

occurrence of material transfer. Therefore, the high temperature wear mechanisms of CS coatings in the air include fatigue, adhesive, and more severe oxidative wear [22,38,39].

The different crystallization and oxidation behavior of CS and HVOF coatings may be the main reason for their different wear rates at 673 K. The contact flash point temperature between the friction sub and the amorphous coating is reported to be related to the ambient temperature, friction coefficient, and material hardness. Compared with CS coating, the lower friction coefficient of HVOF coating at 673 K makes its flash point temperature lower than that of CS coating [40]. As the temperature increases, the contact flash temperature between the friction sub and the coating increases, leading to the crystallization of the wear surface, and the crystallization behavior of the amorphous coating makes the wear region more brittle. Since the plastic toughness of the amorphous alloy significantly affects its wear resistance, the enhancement of brittleness reduces its plastic toughness, which leads to a decrease in wear resistance [18,41].

#### 4. Conclusion

In this work, Fe-based amorphous alloy coatings were prepared on 35CrMo steel substrates utilizing cold spraying and high velocity oxygen fuel spraying techniques. The high temperature frictional wear mechanism of the coatings was investigated at ambient temperatures ranging from room temperature to 673 K. The Fe-based amorphous alloy coating

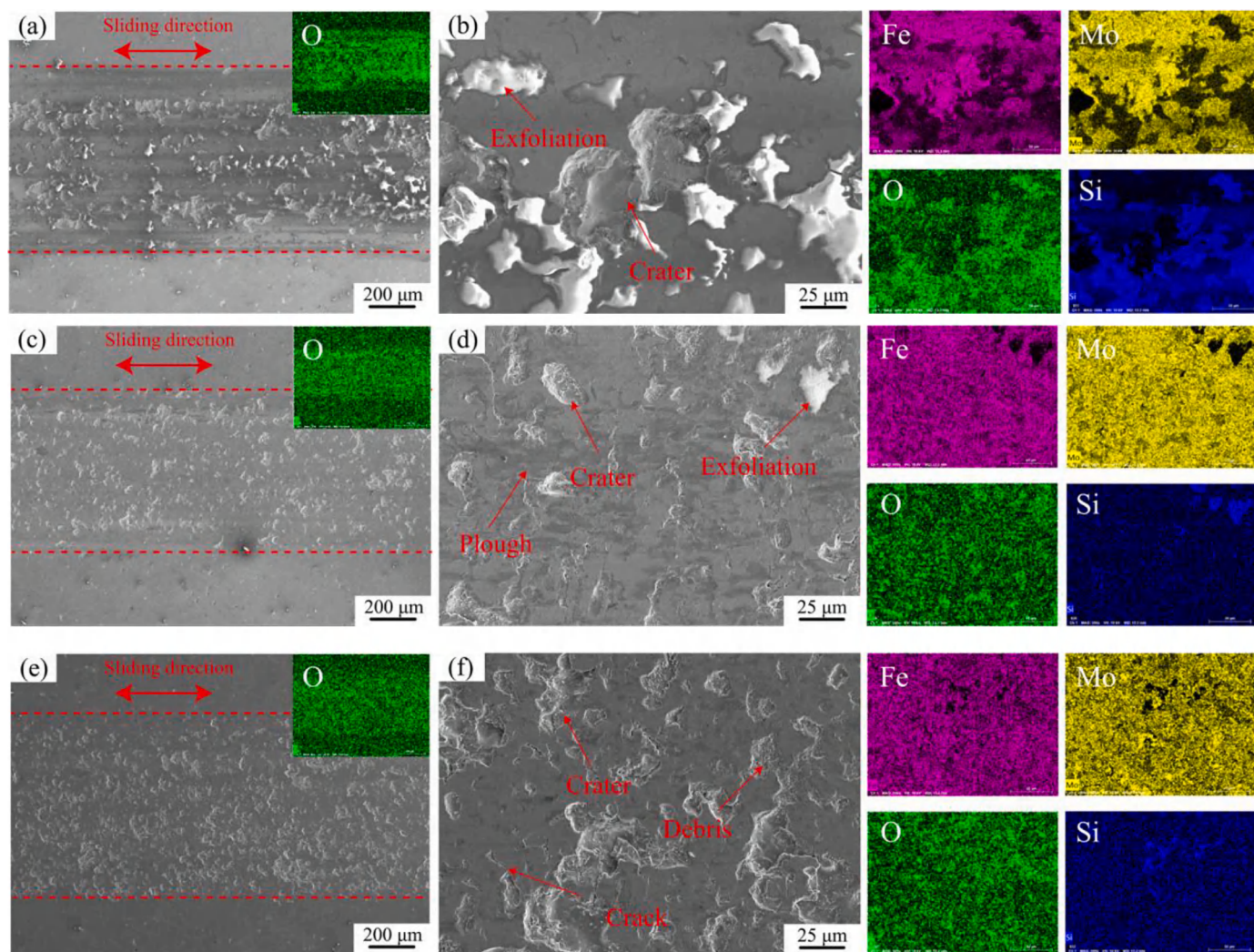


Fig. 11. worn morphologies of HVOF coating under various conditions: (a,b) 293 K; (c,d) 673 K; (e,f) 673 K.

prepared by cold spraying has 90% amorphous content and no obvious crystallization phenomenon. Compared with the HVOF coating, the CS coating has the advantages of high density structure (porosity less than 1.5%), high hardness (Vickers microhardness up to 1104HV0.3), and better thermal stability. At room temperature, the CS coating showed good wear resistance with a wear rate of  $5.59 \times 10^{-6} \text{mm}^3 \cdot \text{m}^{-1} \cdot \text{N}^{-1}$ . At 693 K, the wear resistance of the HVOF coating was better than that of the CS coating with  $1.70 \times 10^{-5} \text{mm}^3 \cdot \text{m}^{-1} \cdot \text{N}^{-1}$ . The wear volume growth rates of the CS coating at 293 K, 473 K, and 673 K were higher than those of the HVOF coatings. Under dry friction wear conditions, the wear rates of Fe-based amorphous alloy coatings all show an increasing trend with the increase of ambient temperature, which is mainly due to the periodic growth, rupture, and peeling of the coating oxide layer under high temperature conditions significantly increasing the wear rates of the coatings. The high temperature wear mechanisms in the air include fatigue, adhesive wear, and more severe oxidation wear.

#### CRediT authorship contribution statement

**Jun-jie Xu:** Data curation, Writing – original draft. **Jia-jie Kang:** Conceptualization, Methodology, Software. **Wen Yue:** Conceptualization, Methodology, Software. **Zhi-qiang Fu:** Supervision. **Li-na Zhu:** Supervision. **Ding-shun She:** Writing – review & editing.

#### Declaration of Competing Interest

We declare that we have no financial and personal relationships with other people or organizations that can inappropriately influence our work, there is no professional or other personal interest of any nature or kind in any product, service and/or company that could be construed as influencing the position presented in, or the review of, the manuscript entitled.

#### Acknowledgements

This project is supported by the National Natural Science Foundation of China (grant no. 41772389), the Pre-Research Program in National 14th Five-Year Plan (grant no. 61409230614), the Tribology Science Fund of State Key Laboratory of Tribology (grant no. SKLTKF19B12), the Fundamental Research Funds for Central Universities (grant no. 2652019069).

#### Supplementary materials

Supplementary material associated with this article can be found, in the online version, at doi:[10.1016/j.jnoncrysol.2021.121136](https://doi.org/10.1016/j.jnoncrysol.2021.121136).

## References

- [1] W. Klement Jun, R.H. Willens, Pol Duwez, Non-crystalline structure in solidified gold-silicon alloys, *Nature* 187 (1960) 869–870.
- [2] D.S. Song, J.H. Kim, E. Fleury, W.T. Kim, D.H. Kim, Synthesis of ferromagnetic Fe-based bulk glassy alloys in the Fe–Nb–B–Y system, *J. Alloys Compd.* 389 (2005) 159–164.
- [3] M.M. Khan, A. Nemati, Z.U. Rahman, U.H. Shah, H. Asgar, W. Haider, Recent advancements in bulk metallic glasses and their applications: a review, *Crit. Rev. Solid State* 43 (2018) 233–268.
- [4] Y.Y. Zhou, G.Z. Ma, H.D. Wang, G.L. Li, S.Y. Chen, H.J. Wang, M. Liu, Fabrication and characterization of supersonic plasma sprayed Fe-based amorphous metallic coatings, *Mater. Des.* 110 (2016) 332–339.
- [5] A. Inoue, B.L. Shen, C.T. Chang, Super-high strength of over 4000 MPa for Fe-based bulk glassy alloys in [(Fe1–xCox)0.75B0.2Si0.05]96Nb4 system, *Acta Mater.* 52 (2004) 4093–4099.
- [6] C. Chang, C. Qin, A. Makino, A. Inoue, Enhancement of glass-forming ability of FeSiBP bulk glassy alloys with good soft-magnetic properties and high corrosion resistance, *J. Alloys Compd.* 533 (2012) 67–70.
- [7] Z. Shi, R. Li, X. Li, C. Wang, T. Zhang, Controllable brittleness in soft-magnetic Fe-PC-B metallic glasses through composition design, *Mater. Sci. Eng. A* 766 (2019), 138385.
- [8] Y. Guo, G.Y. Koga, A.M. Jorge Jr., S. Savoie, R. Schulz, C.S. Kiminami, C. Bolfarini, W.J. Botta, Microstructural investigation of Fe-Cr-Nb-B amorphous/nanocrystalline coating produced by HVOF, *Mater. Des.* 111 (2016) 608–615.
- [9] Q. Luo, Y.J. Sun, J. Jiao, Y.X. Wu, S.J. Qu, J. Shen, Formation and tribological behavior of AC-HVAF-sprayed nonferromagnetic Fe-based amorphous coatings, *Surf. Coat. Technol.* 334 (2019) 253–260.
- [10] A. Kumar, S.K. Nayak, K. Sarkar, A. Banerjee, K. Mondal, L. Lah, Investigation of nano- and micro-scale structural evolution and resulting corrosion resistance in plasma sprayed Fe-based (Fe-Cr-B-C-P) amorphous coatings, *Surf. Coat. Technol.* 397 (2020).
- [11] J.B. Cheng, Y. Feng, C. Yan, X.L. Hu, R.F. Li, X.B. Liang, Development and characterization of Al-based amorphous coating, *JOM* 72 (2020) 745–753.
- [12] J. Henaou, A. Concustell, I.G. Cano, N. Cinca, S. Dosta, J.M. Guilemany, Influence of Cold Gas Spray process conditions on the microstructure of Fe-based amorphous coatings, *J. Alloys Compd.* 622 (2015) 995–999.
- [13] J. Su, J.J. Kang, W. Yue, G.Z. Ma, Z.Q. Fu, L.N. Zhu, D.S. She, H.D. Wang, C. B. Wang, Review of cold spraying and its use for metallic glass coatings, *Mater. Sci. Technol. Lond.* 35 (2019) 1908–1923.
- [14] M. Yasir, C. Zhang, W. Wang, P. Xu, L. Liu, Wear behaviors of Fe-based amorphous composite coatings reinforced by Al<sub>2</sub>O<sub>3</sub> particles in air and in NaCl solution, *Mater. Des.* 88 (2015) 207–213.
- [15] J. Su, J.J. Kang, W. Yue, G.Z. Ma, Z.Q. Fu, L.N. Zhu, D.S. She, H.D. Wang, C. B. Wang, Comparison of tribological behavior of Fe-based metallic glass coatings fabricated by cold spraying and high velocity air fuel spraying, *J. Non-Cryst. Solids* 522 (2019), 119582.
- [16] Z. Zhou, L. Wang, F.C. Wang, H.F. Zhang, Y.B. Liu, S.H. Xu, Formation and corrosion behavior of Fe-based amorphous metallic coatings by HVOF thermal spraying, *Surf. Coat. Technol.* 204 (2009) 563–570.
- [17] C.C. Sun, X.L. Zhou, C. Xie, Effect of processing conditions on Al-based amorphous/nanocrystalline coating by cold-spraying, *Surf. Coat. Technol.* 362 (2019) 97–104.
- [18] J. Kong, D.S. Xiong, J.L. Li, Q.X. Yuan, R. Tyagi, Effect of flash temperature on tribological properties of bulk metallic glasses, *Tribol. Lett.* 35 (2009) 151–158.
- [19] H. Guo, S.D. Zhang, W.H. Sun, J.Q. Wang, Differences in dry sliding wear behavior between HVAF-sprayed amorphous steel and crystalline stainless steel coatings, *J. Mater. Sci. Technol.* 35 (2019) 865–874.
- [20] X.L. Ji, S.H. Alavi, S.P. Harimkar, High-temperature sliding wear behavior of Zr-based bulk amorphous alloys, *JOM* 67 (2015) 1578–1584.
- [21] X.Q. Li, H.M. Zhai, W.S. Li, S. Cui, W.C. Ning, X.L. Qiu, Dry sliding wear behaviors of Fe-based amorphous metallic coating synthesized by D-gun spray, *J. Non-Cryst. Solids* 537 (2020), 120018.
- [22] D.D. Liang, J. Ma, Y.F. Cai, X.D. Liu, S.D. Xie, X.S. Wei, G. Xu, J. Shen, Characterization and elevated-temperature tribological performance of AC-HVAF-sprayed Fe-based amorphous coating, *Surf. Coat. Technol.* 387 (2020), 125535.
- [23] A.L. Greer, K.L. Rutherford, M. Hutchings, Wear resistance of amorphous alloys and related materials, *Int. Mater. Rev.* 47 (2002) 87–112.
- [24] S. Yugeswaran, A. Kobayashi, K. Suresh, K.P. Rao, B. Subramanian, Wear behavior of gas tunnel type plasma sprayed Zr-based metallic glass composite coatings, *Appl. Surf. Sci.* 258 (2012) 8460–8468.
- [25] M R Rokni, S R Nutt, C A Widener, et al., Review of relationship between particle deformation, coating microstructure, and properties in high-pressure cold spray, *J. Therm. Spray Tech.* 26 (2017) 1308–1355.
- [26] Z Y Piao, Z Y Zhou, J Xu, et al., Use of X-ray computed tomography to investigate rolling contact cracks in plasma sprayed Fe-Cr-B-Si coating, *Tribol. Lett.* 67 (2019) 11.
- [27] S D Zhang, W L Zhang, S G Wang, et al., Characterisation of three-dimensional porosity in an Fe-based amorphous coating and its correlation with corrosion behavior, *Corros. Sci.* 93 (2015) 211–221.
- [28] J.S. Keist, T.A. Palmer, Development of strength-hardness relationships in additively manufactured titanium alloys, *Mater. Sci. Eng. A* 693 (2017) 214–224.
- [29] X.B. Liang, J.C. Shang, Y.X. Chen, Z.D. Zhou, Z.B. Zhang, B.S. Xu, Influence of ceramic particles and process parameters on residual stress of flame-sprayed Fe based coatings, *Surf. Coat. Tech.* 354 (2018) 10–17.
- [30] A. Inoue, Stabilization of metallic supercooled liquid and bulk amorphous alloys, *Acta Mater.* 48 (2000) 279–306.
- [31] I. Nogueira, A.M. Dias, R. Gras, R. Progrid, An experimental model for mixed friction during running-in, *Wear* 253 (2002) 541–549.
- [32] Z. Li, C. Zhang, L. Liu, Wear behavior and corrosion properties of Fe-based thin film metallic glasses, *J. Alloys Compd.* 650 (2015) 127–135.
- [33] C.X. Xie, W. Li, F.H. Shen, Y. Liu, L. Xie, Z.L. Liao, S.Y. Zhong, Plastic deformation behavior of a novel Fe-based metallic glass under different mechanical testing techniques, *J. Non-Cryst. Solids* 499 (2018) 58–61.
- [34] Z. Zhou, L. Wang, D.Y. He, F.C. Wang, Y.B. Liu, Microstructure and wear resistance of Fe-based amorphous metallic coatings prepared by HVOF thermal spraying, *J. Therm. Spray Tech.* 19 (2010) 1287–1293.
- [35] B.S. Zhang, J.B. Cheng, X.B. Liang, Effects of Cr and Mo additions on formation and mechanical properties of arc-sprayed FeBSiNB-based glassy coatings, *J. Non-Cryst. Solids* 499 (2018) 245–251.
- [36] C. Zhang, L. Liu, K.C. Chan, Q. Chen, C.Y. Tang, Wear behavior of HVOF-sprayed Fe-based amorphous coatings, *Intermetallics* 29 (2012) 80–85.
- [37] S. Yoon, C. Lee, H. Choi, Evaluation of the effects of the crystallinity of kinetically sprayed Ni–Ti–Zr–Si–Sn bulk metallic glass on the scratch response, *Mat. Sci. Eng.: A* 449–451 (2007) 285–289.
- [38] H.R. Ma, X.Y. Chen, J.W. Li, C.T. Chang, G. Wang, H. Li, X.M. Wang, R.W. Li, Fe-based amorphous coating with high corrosion and wear resistance, *Surf. Eng.* 33 (2017) 56–62.
- [39] J. Cheng, D. Liu, X. Liang, Y. Chen, Wear behaviors of arc-sprayed FeBSiNB amorphous coatings, *Tribol. Lett.* 60 (2015) 22.
- [40] Y. Liu, A. Erdemir, E.I. Meletis, A study of the wear mechanism of diamond-like carbon films, *Surf. Coat. Tech.* 82 (1996) 48–56.
- [41] Z.L. Liao, N.B. Hua, W.Z. Chen, Y.T. Huang, T. Zhang, Correlations between the wear resistance and properties of bulk metallic glasses, *Intermetallics* 93 (2018) 290–298.